Pure Appl. Geophys. 175 (2018), 1525–1543

https://doi.org/10.1007/s00024-017-1745-1

Pure and Applied Geophysics

Airburst-Generated Tsunamis

Marsha Berger[1] and Jonathan Goodman[1]

Abstract—This paper examines the questions of whether smaller asteroids that burst in the air over water can generate tsunamis that could pose a threat to distant locations. Such airburst-generated tsunamis are qualitatively different than the more frequently studied earthquake-generated tsunamis, and differ as well from tsunamis generated by asteroids that strike the ocean. Numerical simulations are presented using the shallow water equations in several settings, demonstrating very little tsunami threat from this scenario. A model problem with an explicit solution that demonstrates and explains the same phenomena found in the computations is analyzed. We discuss the question of whether compressibility and dispersion are important effects that should be included, and show results from a more sophisticated model problem using the linearized Euler equations that begins to addresses this.

Key words: Tsunami, asteroid-generated airburst, shallow water equations, linearized Euler equations.

1. Introduction

In Feb. 2013, an asteroid with a 20 m diameter burst 30 km high in the atmosphere over Chelyabinsk, causing substantial local damage over a 20,000 km^2 region (Popova et al. 2013). The question arises what would be the effect of an asteroid that bursts over the ocean instead of land? The concern is that the atmospheric blast wave might generate a tsunami threatening populated coastlines far away.

There is little literature on airburst-generated tsunamis. Most of the literature on asteroids study the more complicated case of water impacts, where the meteorite splashes into the ocean (Weiss et al. 2006; Gisler et al. 2010; Gisler 2008). This involves much more complicated physics. The only reference we are aware of that relates to a blast-driven water wave is from the 1883 volcanic explosion of Krakatoa (Harkrider and Press 1967). The authors report a tide gauge in San Francisco registered a wave that could not be explained by a tsunami. There is also some analytic work in Kranzer and Keller (1959), where they derive asymptotic formulas for water waves from explosions and from initial cavities. There is more literature on meteo-tsunamis. These are also driven by air-pressure events and have similarities to our case, but occur in a different regime of air speed and water depth.

This paper studies the behavior of airburst-generated tsunamis, to better understand the potential threat. We compute the ocean response to a given (specified or pre-computed) atmospheric overpressure. The ocean response to this overpressure forcing, including the possible tsunami, is simulated. Typically, the shallow water equations are used for long-distance propagation, since they efficiently and affordably propagate waves over large trans-oceanic distances. Other alternatives, such as the Boussinesq equations, are much more expensive, and at least for the case of earthquake-generated tsunamis the difference seems to be small (Liu 2009).

In the first part of the paper, we present simulations under a range of conditions using the shallow water equations and the GeoClaw software package (GeoClaw 2017). We compute the ocean's response to an overpressure as calculated in Aftosmis et al. (2016). The overpressure was found by simulating the blast wave in air, and extracting the ground footprint. Roughly speaking, the blast wave model corresponds to the largest meteor that deposits all of its energy in the atmosphere without actually reaching the water surface. With this forcing, if there is no sizeable response, then we can conclude that that airbursts do not effectively transfer energy to the ocean, and there is little threat of distant inundation.

[1] Courant Institute, New York University, 251 Mercer St., New York City, NY 10012, USA. E-mail: berger@cims.nyu.edu

In general, our results using the shallow water equations suggest that airburst-generated tsunamis are too small to cause much coastal damage. Of course, depending on local bathymetry there could be an unusual response that is significant. For example, Crescent City, California is well known to be subject to inundation due to the configuration of its harbor and local bathymetry. However, we find that to generate a large enough response so that the water floods the coastline, the blast has to be so close that the blast itself is the more dangerous phenomenon. This is also the conclusion reached by Gisler et al. (2010) and Melosh (2003) for the case of asteroid water impacts.

In the second part of this paper, we study model problems to better understand and describe the phenomena we compute in the first part. The first model problem is based on the one-dimensional shallow water equations for which we can obtain an explicit closed form solution. It assumes a traveling wave form for the pressure forcing. Actual blast waves only approximately satisfy this hypothesis for a short time before their amplitudes decay. Nevertheless, the model explains several key features that we observe in the two-dimensional simulations. We observe a response wave that moves with the speed of the atmospheric forcing. There is also the gravity wave, or tsunami, moving at the shallow water wave speed c_w that is generated by the initial transient of the atmospheric forcing. We study in detail the response wave, or 'forced' wave, but the two are closely related. The analysis shows that the forced wave is proportional to the local depth of the water h at each location, a phenomena clearly seen in our computations. The model problem also allows us to assess the importance of nonlinear modeling. For most physical situations related to airburst tsunamis, the linear and nonlinear models give similar predictions.

In our final section, we assess the effect of corrections to the shallow water equations arising from compressibility and dispersion using a second model problem—the linearized Euler equations. Airbursts have much shorter time and length scales than the earthquakes that generate tsunamis, comparable to the acoustic travel time to the ocean floor. This leads to the question of whether compressibility of the ocean water could be a significant factor. In addition, airbursts have much shorter wavelengths, on the order of 10–20 km, at least for meteors with diameter less than 200 m or so. Recall that the shallow water model results from assuming long wavelengths and incompressibility of the water. Our results show that for airburst-generated tsunamis, dispersion can be significant but that compressibility is less so, suggesting interesting avenues for future work.

This work is an outgrowth of the 2016 NASA-NOAA Asteroid-generated Tsunami and Associated Risk Assessment Workshop. The workshop conclusions are summarized in Morrison and Venkatapathy (2017). Several other researchers also performed simulations, and videos of all talks are available online.[1]

2. *Two-Dimensional Simulations*

In this section, we present results from two sets of simulations. We use a 250MT blast, which roughly corresponds to a meteor with a 200 m diameter entering the atmosphere with a speed of 20 km/s. Generally speaking, this is the largest asteroid that would not splash into the water.[2] For each location, we did several simulations varying the blast locations with no meaningful difference in results, so we only present one representative computation in each set of simulations.

In the first set of results, we locate the blast in the Pacific about 180 km off the coast of near Westport, Washington. This spot was chosen since it is well studied by the earthquake-generated tsunami researchers due to its proximity to the M9 Cascadia fault (Petersen et al. 2002; Gica et al. 2014). By the time the waves reach shore, they have decayed and are under a meter high. Since they do not have the long length scales of earthquake tsunamis, we did not see any inundation on shore. In the second set of results, we move the location offshore to Long Beach,

[1] All presentations are available at https://tsunami-workshop.arc.nasa.gov/workshop2016/sched.php

[2] Initially, we used a blast wave corresponding to a 100MT blast, but since no significant response was found we do not include those results here. We also did simulations where we increased the 250MT pressure forcing by a factor of 1.2 with no change to the conclusions.

California, where there is significant coastal infrastructure, and has also been studied extensively in relation to earthquake tsunamis (Uslu et al. 2010). We place the blast approximately 30 km from shore, so that there is less time for the waves to decay. In all simulations, bathymetry is available from the NOAA National Center for Environmental Information website.

To perform these simulations, we use a model of the blast wave simulated in Aftosmis et al. (2016). The ground footprint for the overpressure was extracted, a Friedlander profile was fit to the data, and its amplitude as a function of time was modeled by a sum of Gaussians. The 250MT model is shown in Fig. 1, with a few of the profiles drawn in black to illustrate their form. The profiles start with the rise in pressure from the incoming blast, and are followed by the expected rarefaction wave (underpressure) some distance behind. Note that the maximum amplitude is over four atmospheres, but decays rapidly from its initial peak. In the model, the blast wave travels at a fixed speed of 391 m/s. If we take the sound speed at sea level to be 343 m/s, this corresponds to a Mach 1.14 shock.. This may be less accurate at early times. If the asteroid enters at a low angle of incidence, the blast wave travels more quickly when it first hits the ground. This would also lead to a more anisotropic response when see from the ground. Here, however, we assume that the blast wave is radially symmetric. We then use this model of the overpressure as a source term in our two-dimensional shallow water simulations using the software package `GeoClaw`.

`GeoClaw` is an open source software package developed since 1994 (LeVeque et al. 2011) for modeling geophysical flows with bathymetry using the shallow water equations. It is mostly used for simulations of tsunami generation, propagation and inundation. `GeoClaw` uses a well-balanced, second-order finite volume scheme for the numerics (LeVeque 1997; George 2008). Some of the strengths of `GeoClaw` include automatic tracking of coastal inundation, robustness in its handling of dry states, a local adaptive mesh refinement capability, and the automated setup that allows for multiple bathymetry input files with varying resolution. A bottom friction term is included using a constant Manning coefficient of 0.025. The results below do not include a Coriolis force, which we have found to be unimportant. There is no dispersion in the shallow water equations. In 2011, the code was approved by the US National Tsunami Hazard Mitigation Program (NTHMP) after an extensive set of benchmarks used to verify and validate the code (González 2012).

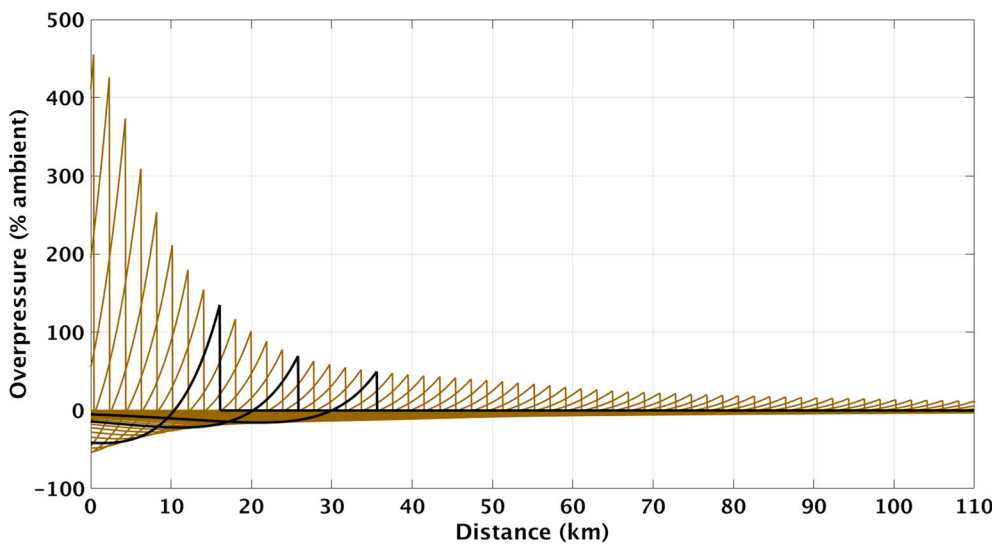

Figure 1
Ground footprint for 250MT blast wave overpressure as a function of distance from the initial blast. The curves are drawn every 5 s. A few of the curves are drawn in black to more clearly show a typical Friedlander profile

2.1. Westport Results

For this set of simulations, the 250MT blast is located at -126.25° longitude and 46.99° latitude, about 30 km from the continental slope. The ocean is 2575 m deep at this spot. The blast location is about 180 km from shore. Many simulations were performed with different mesh resolutions. The finest grids used in the adaptive simulations had a resolution of 1/3 arc second. Three bathymetric data sets were used—a 1 min resolution covering the whole domain, a 3 s resolution nearer shore, and a 1/3 arc second bathymetry that included the shoreline itself.

In Fig. 2, we show a Hovmöller plot through the center of the blast location at a fixed latitude. On the left is the atmospheric overpressure for the first 300 s. This is the forcing that travels at 391 m/s. On the right is the amplitude of the water's response. Two waves traveling at different speeds are visible. A shallow water gravity wave travels with speed $c_w \approx \sqrt{gh}$ which at the blast location is 158 m/s. It is evident that the blast wave travels approximately twice as fast as the gravity wave. The blast wave reaches the edge of the graph in just over 150 s instead of the 300 s of the main water wave (in blue, since it is a depression). Also visible in the wave height plot is a wave that starts off in red and travels at the same speed as the blast wave, and whose amplitude decays more rapidly. Here, the color scale saturates below the maximum value in each plot so that smaller waves are visible.

Figure 3 shows the maximum amplitude found at any time in the simulation at that location. Note that the color bar is not linear in this plot, so that the different levels can more easily be seen. Nearest the blast location the maximum wave amplitude is over 10 m, but it decay rapidly. As the waves approach shore, the waves are amplified in a non-uniform way by the bathymetry. The coastline is outlined in black. We do not see any inundation of land, although admittedly at this resolution it would be hard to see.

Figure 4 shows the time history of wave heights through several gauge plots. The left plot shows seven gauges placed 0.1° apart (about 10 km at this latitude), starting about 1 km from the blast and at the same latitude. The gauge closest to the blast location has a maximum amplitude that reaches 5 m. Subsequent gauges show a very rapid decay in maximum amplitude. These positive elevation waves are the water's response to the blast wave overpressure, and travel at the same speed as the blast wave. Most of

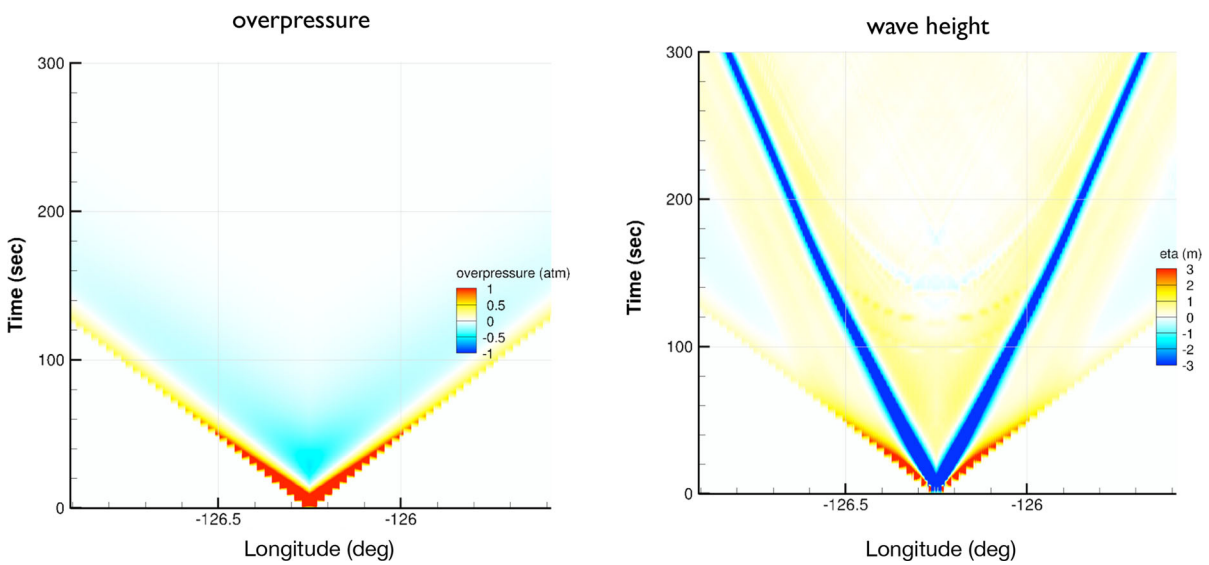

Figure 2
The Hovmöller plot shows the overpressure in atmospheres through the center of the blast location (left) and the wave height (right). The blast wave speed is approximately twice the gravity wave speed, and its amplitude decays more rapidly

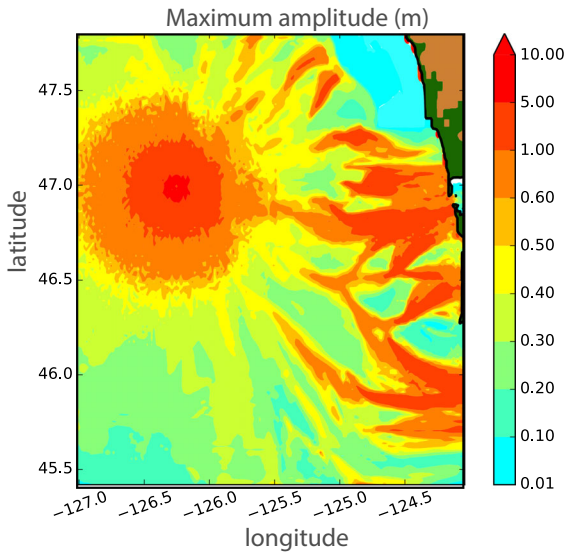

Figure 3
Maximum amplitude found between the blast location and the shoreline during the simulation. Note the color scale is not equally spaced

the ocean's response at this location appears as a depression, not an elevation. The negative amplitude wave travels at the gravity wave speed, $\sqrt{gh}$, where the water has depth h. It shows much less decay in amplitude. For example, looking at gauge 3 and 5, the peak amplitude decays from 2.7 to 0.72 m in about 50 s, whereas between 100 and 200 s, the trough decays from −5.3 to −4.1 m in about 100 s.

Figure 4 right shows gauges approaching the shore, at latitude 46.88° so that it lines up with the opening to Gray's Harbor. The gauges start about 100 km away from the blast. These are not equally spaced but are placed from 0.25 to 0.1° apart (from 25 to 10 km at this latitude), becoming closer as they approach shore and the bathymetry changes more rapidly. Shoaling is observed as the wave amplitudes increase, seen in gauges 17 and higher. The maximum elevation is between 0.5 and 1 m, and its duration is short, at least compared to earthquake-generated tsunamis.

Finally, Fig. 5 shows several close-ups of the region near shore. The waves are of uneven strength due to focusing from the bathymetry. The maximum amplitude is around 1 m. The sequence shows waves reflecting from the coastline but not flooding it. Some waves enter Grays Harbor, but they small amplitude and do not flood the inland area either.

2.2. *Long Beach Results*

For this set of experiments, we move the simulations to Long Beach, California. We locate the blast very close to shore so that the waves do not have time

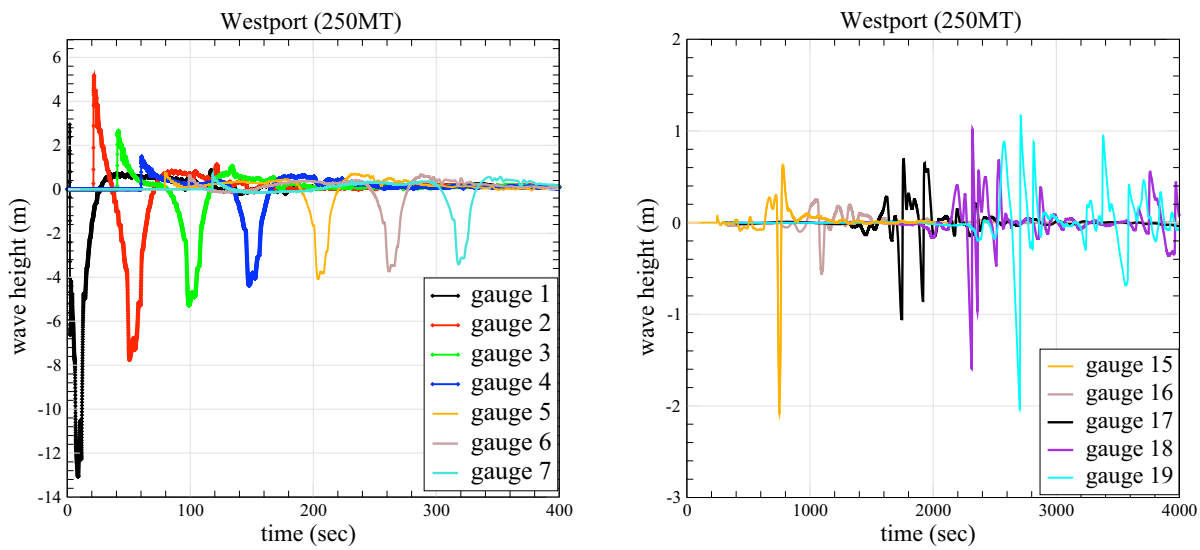

Figure 4
(Left) Gauges near blast location, every 0.1° starting 0.01° from blast. Gauges show rapid decay of maximum amplitude, much slower decay of maximum depressions. (Right) Gauges approaching shoreline show similar wave forms with decreasing maximum amplitude before shoaling increases it. These gauge locations are marked in Fig. 5

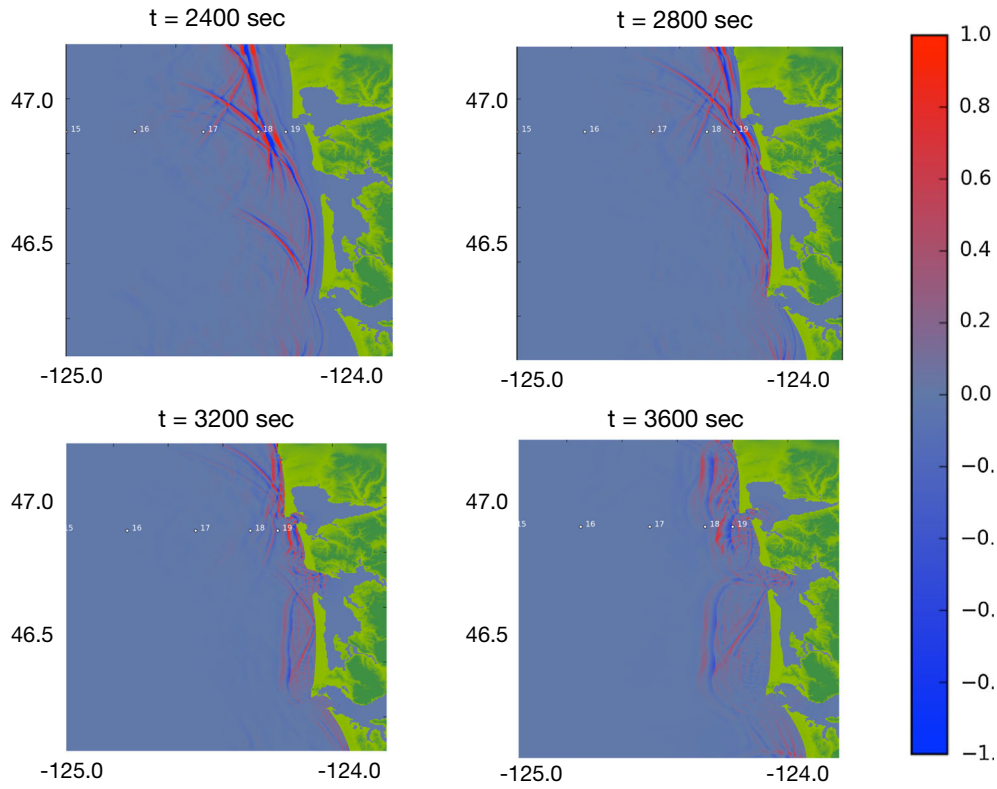

Figure 5
Zoom of waves approaching shoreline around Westport. No inundation is observed

to decay. Again we have detailed bathymetry at a resolution of 1/3 arc second between Catalina Island and Long Beach, and use a 1 min dataset outside of this region. The blast is located at $-118.25°$ longitude and $33.41°$ latitude, where the ocean is 797 m deep. This is about 30 km from shore. Figure 6 shows the region where the blast is located, and a zoom of the Long Beach harbor where we will look for flooding.

Figure 7 shows the ocean response at several points in time. The black circle on the plots indicates the location of the air blast. In the plot marked at 25 s, note how the wave height in red that is closest to the blast location is not as circular as the air blast itself. It also decays faster than in the Westport computation. This will be explained by the model problem presented in the next section.

There is a breakwater that protects Long Beach. It reflects most of the waves that reach it, with only a small portion getting through the opening. Waves that reach the harbor go around the breakwater, and are reflected from the shoreline back into this region.

Figure 8 shows a plot of the maximum water amplitudes seen in the harbor area. We do see some overtopping of land, but it is very small. In several locations, it reaches 0.5 m, where the inlet exceeds its boundaries, and on the dock in the middle. The region with the largest accumulation is just outside the harbor before the breakwater, where the maximum amplitude seen is between 3 and 6 m. There is a steep cliff here, however, and the water does not propagate inland. Paradoxically, in other experiments where the blast was located closer to shore by a factor of 2, there was no overtopping. This can also be explained by our model problem in the next section.

3. *Shallow Water Model*

In this section, we present a one-dimensional model of the shallow water equations (SWE) that explains much of the behavior seen in the previous

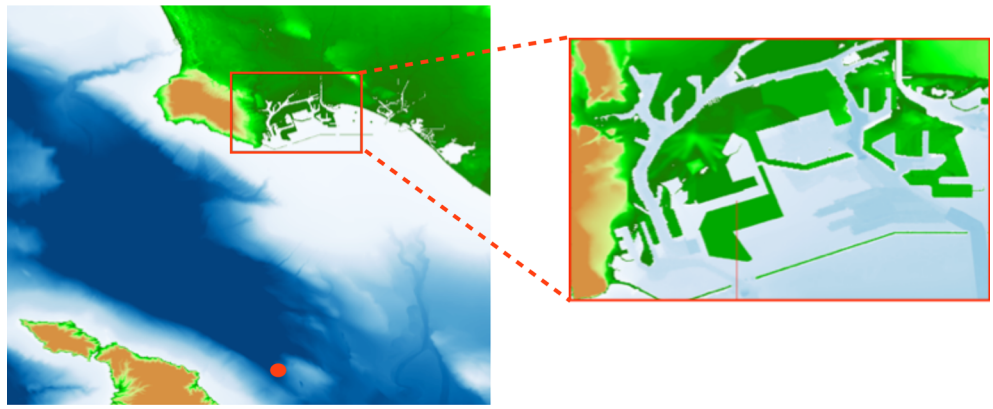

Figure 6
Location of airburst northeast of Catalina, and zoom of Long Beach shoreline

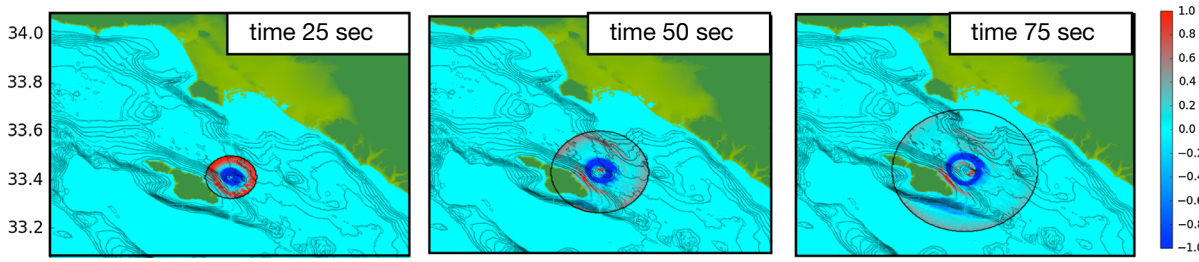

Figure 7
Snapshots at early times of blast wave and ocean waves in Long Beach simulation

examples. In the SWE, the atmospheric overpressure appears as an external forcing p_e in the momentum equation. In one space dimension, it is

$$\begin{aligned} h_t + (hu)_x &= 0, \\ (hu)_t + (hu^2 + \frac{1}{2}gh^2)_x &= \frac{-h\,p_{ex}}{\rho_w}, \end{aligned} \tag{1}$$

where h is the height of the water surface over the bottom, u is the depth-averaged velocity of the water in the x direction, g is gravity, and ρ_w is the density of water. The external pressure forcing is p_e, and its x derivative is p_{ex}. The notation is illustrated in Fig. 9. We assume constant bathymetry in the model, $B(x,t) = 0$. See Vreugdenhil (1994) for these equations, or Mandli (2011) for a clear and complete derivation. In this section (and the next), the conclusions are in the last few paragraphs after the analysis.

3.1. Derivation and Analysis

As stated in the introduction, we simplify the pressure forcing by assuming it has the form of a traveling wave, and look for solutions h and u that are traveling waves too. This means they are functions only of the moving variable

$$m = x - st\ .$$

so that $\partial_t h = -s\,\partial_m h(x - st) = -s\,h_m$. Equation (1) becomes a pair of ordinary differential equations

$$-sh_m + (hu)_m = 0, \tag{2}$$

$$-s(hu)_m + (hu^2 + \frac{1}{2}gh^2)_m = \frac{-hp_{em}}{\rho_w}\ . \tag{3}$$

Equation (2) can be integrated to give $-sh + hu =$ const . We evaluate the constant by

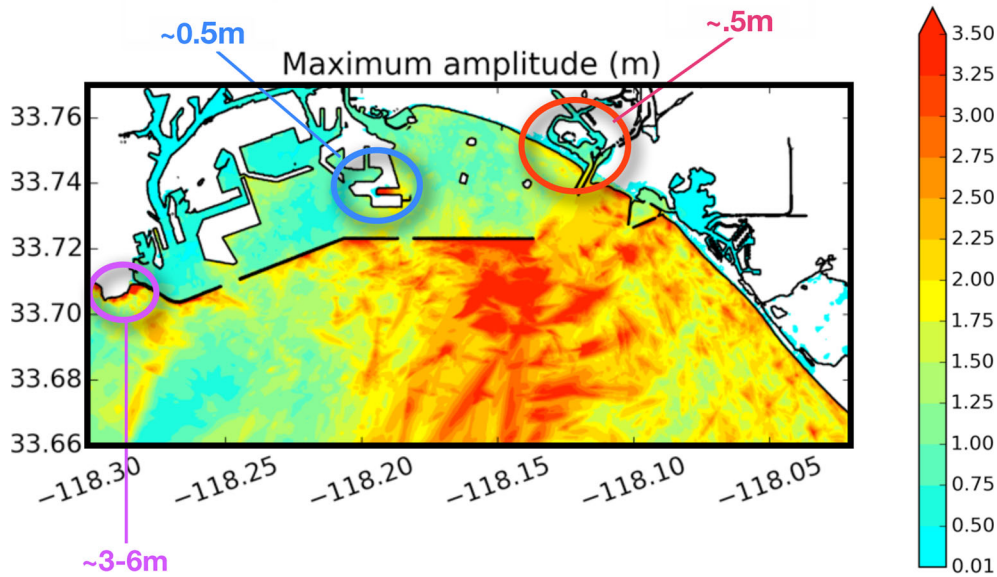

Figure 8
Maximum amplitude plot shows 0.5 m of water overtopping the dock and the riverbank

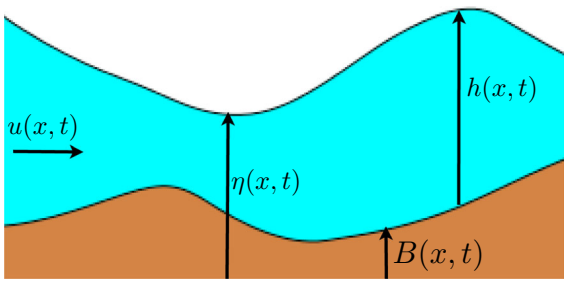

Figure 9
Illustration of variables for Eq. (1). In the general case, the bathymetry $B(x, t)$ varies in space and possibly time. Here, we take it to be constant

taking $m \to \infty$, where $u \to 0$ and $h \to h_0$, with h_0 the undisturbed water height. (We assume that the overpressure has localized support, and goes to zero as $m \to \infty$.) Therefore, $-sh + hu = -sh_0$. This may be re-written as:

$$u(m) = \frac{s(h(m) - h_0)}{h(m)} \ .$$

We use this to eliminate u from (3), which gives

$$-s\left(s(h - h_0)\right)_m + \left(\frac{s^2(h - h_0)^2}{h}\right)_m + \left(\frac{1}{2}gh^2\right)_m = \frac{-hp_{em}}{\rho_w} \ .$$

After some algebra, this leads to

$$\frac{s^2}{2}\left(\frac{h_0^2}{h^2}\right)_m + g\,h_m = \frac{-p_{em}}{\rho_w} \ . \tag{4}$$

As before, this may be integrated exactly. Again we use the boundary conditions $h \to h_0$, $u \to 0$, and $p_e \to 0$ as $m \to \infty$. The result is

$$\frac{s^2}{2}\left(1 - \frac{h_0^2}{h(m)^2}\right) + gh_0\left(1 - \frac{h(m)}{h_0}\right) = \frac{p_e(m)}{\rho_w} \ . \tag{5}$$

To summarize, Eq. (5) is the water's response according to shallow water theory. The solution of the differential equation system (2) and (3) is an algebraic relation between the overpressure and the response height. It tells us that the water height at a point $m = x - st$ is determined by the overpressure at the same point.

To get a better feel for the behavior of the solution (5), we linearize it, writing $h(m) = h_0 + h_r(m)$ where $h_r(m)$ is the response height. The linearization uses the relation

$$\left(\frac{h_0}{h(m)}\right)^2 = \frac{h_0^2}{(h_0 + h_r)^2} \approx 1 - \frac{2h_r}{h_0} \ ,$$

which is valid when $h_r \ll h_0$. This is our case, since the change in wave height h_r is a number in meters

where h_0 is typically measured in kilometers. The linearization of (5) is

$$h_r = \frac{h_0\, p_e}{\rho_w (s^2 - c_w^2)} \ . \tag{6}$$

Figure 10 shows that the full response theory (5) and the linear approximation (6) are very close to each other for the parameters of interest. The plot uses a constant depth of $h_0 = 4$ km, and takes $\rho_w = 1025$ kg / m ^{3}. The maximum difference between the nonlinear and linear wave heights in Fig. 10 is half a meter, less than 2%, when the overpressure is five atmospheres.

To enumerate the consequences of the response predicted by (5) and (6), we observe

1. The response wave height h_r is linearly proportional to the depth h_0. A pressure wave over deep ocean has a stronger effect than a pressure wave over a shallower continental shelf. This explains why locating the blast in the Long Beach case closer to shore had less of an effect. If the distance offshore of the air blast from Long Beach is halved to 15 km, the ocean is only 90 m deep, resulting in approximately 1/10 the impact response. On the other hand, there is almost no difference in the decay rate of the shallow water waves before they reach shore.
2. If $s > c_w$, then p_e and h_r have the same sign. The response height is positive in regions of positive overpressure. This contradicts an intuition that positive overpressure would depress the water surface. This response is similar to the case of a forced oscillator in vibrational analysis. Consider for example $\ddot{x} = -x + A\cos(\omega t)$. The steady solution is

$$x(t) = \frac{A}{1-\omega^2}\cos(\omega t)\,.$$

For $\omega > 1$, the response $x(t)$ has the opposite sign from the forcing $A\cos(\omega t)$. For pressure forcings with speeds slower than the water speed, the water response would be a depression, with h_r negative. This response is clearly seen in the all the simulations. The wave that travels at the speed of the blast wave is an elevation. However, in the Long Beach results, we can see that the response wave is not uniformly circular when the depth of the water changes rapidly. Note that if we take the speed of sound in air is 343 m/s, the water would have to be more than 12 km deep for the gravity wave speed to exceed the speed of the pressure forcing. So in all cases on earth we expect an elevation of the sea surface beneath the pressure wave.

3. The response is particularly strong when the forcing speed s is close to the gravity wave speed $c_w \approx 200$ m/s., (for $h_0 = 4$ km). In this case, we have a Proudman resonance (Proudman 1929; Monserrat et al. 2006). This is the regime for meteo-tsunamis, in basins whose depth leads to

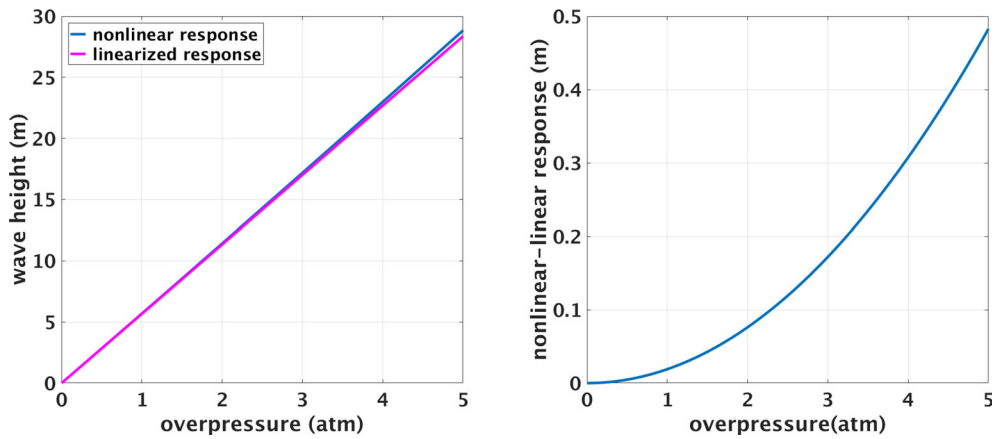

Figure 10
Wave height as a function of overpressure, for the nonlinear Eq. (5) and the linearized Eq. (6), using $h_0 = 4$ km and $s = 350$ m/s. The curves are very close. The right figure is a plot of their difference, which is on the order of a percent

gravity wave speeds that match the squall speeds. These speeds are much slower than the speed of sound in air.

3.2. Shallow Water Model Computations

This subsection presents solutions of the one dimensional model (1) computed using `GeoClaw`. These show the generation of freely propagating gravity waves along with the forced response wave described above. The sealevel and bathymetry are taken to be flat for $t \le 0$, so the initial conditions for this simulation are $h = 0$ and $u = 0$ at $t = 0$. For $t \ge 0$, the pressure forcing is

$$\begin{aligned} p_e &= p_{\text{ambient}} \exp(-0.1(x - st)^2) \\ &= p_{\text{ambient}} \exp\left(-\frac{1}{2}\left(\frac{x - st}{\sqrt{5}}\right)^2\right), \end{aligned} \tag{7}$$

with p_{ambient} = 1 atm. One can check that the solution to the linearized equations is

$$\begin{aligned} h(x,t) = h_r(x - st) &- \left(\frac{s}{c_w} + 1\right)\frac{h_r(x - c_w t)}{2} \\ &+ \left(\frac{s}{c_w} - 1\right)\frac{h_r(x + c_w t)}{2}, \end{aligned} \tag{8}$$

The computed solution to the nonlinear equation is very close to this. It corresponds to the response wave moving to the right, and two gravity waves. Conservation of water requires that the sum of the amplitudes is zero:

$$1 - \frac{1}{2}\left(\frac{s}{c_w} + 1\right) + \frac{1}{2}\left(\frac{s}{c_w} - 1\right) = 0\,. \tag{9}$$

The gravity waves move at the shallow water speed $c_w = \sqrt{gh_0}$. The forced wave (what we have been calling the response wave) moves with speed s.

These initial conditions have a non-zero air blast pressure wave only at time $t > 0.0$. It is not a pure traveling wave, since the forcing p_e is zero before $t = 0.0$. The general solution to this linearized shallow water model is a combination of the inhomogeneous solution with forcing function p_e, which gives the response wave h_r, and the solution to the homogeneous problem with $p_e = 0$, which consists of left and right moving gravity waves of the same shape h_r but different amplitudes. The full solution is a linear combination of all three waves that satisfy the initial conditions. Equation (8) shows that the left-going tsunami wave (rightmost term) will have a smaller amplitude in absolute value for $s/c_w > 1$ than the right going wave (middle term on right hand side). Also, the latter will be a depression, since it has amplitude $-0.5 \cdot (1 + s/c_w))$.

Numerical results illustrating this are shown in Fig. 11 at time 250 s. Solid lines show the water wave heights, and dashed lines show the air overpressure profiles. In Fig. 11 left, the speed $s = 350$ m/s, somewhat larger than the speed of sound in air. For this case, since $s > c_w$, (for h_0 = 4 km, $c_w = \sqrt{gh_0} \simeq 198$ m/s), the forced wave height is positive since the overpressure is positive. Note that the gravity wave at the same point in time trails the pressure wave. The right-moving gravity wave is a depression, the left moving wave is a smaller elevation. Since this calculation is in one space dimension, the waves do not decay. In the two-dimensional shallow water equations, the gravity wave decays with the square root of distance. Also, the pressure blast wave and, therefore, the leading water response would both decay too.

By contrast, Fig. 11 right shows the water's response for an overpressure moving at 120 m/s, slower than the gravity wave ($s < c_w$). The tsunami waves travel at the same speed in both computations, but they have different amplitudes and signs. The tsunami wave is the opposite sign as the wave due to the pressure. This is consistent with conservation of mass.

To give a more complete picture, two more experiments with $s > c_w$ but different forcings are shown in Fig. 12. The figures on the left use a Gaussian pressure forcing but their magnitude is ramped up for the first 100 s. This results in quite a different-looking gravity wave. The right figure uses a typical Friedlander blast profile described in Sect. 2 for the overpressure, but keeping the amplitude constant at 1 atm. It looks similar to the Gaussian example above.

3.3. Breakdown of Smooth Solutions

In a bit of a digression, this subsection examines in a little more detail the nonlinear shallow water

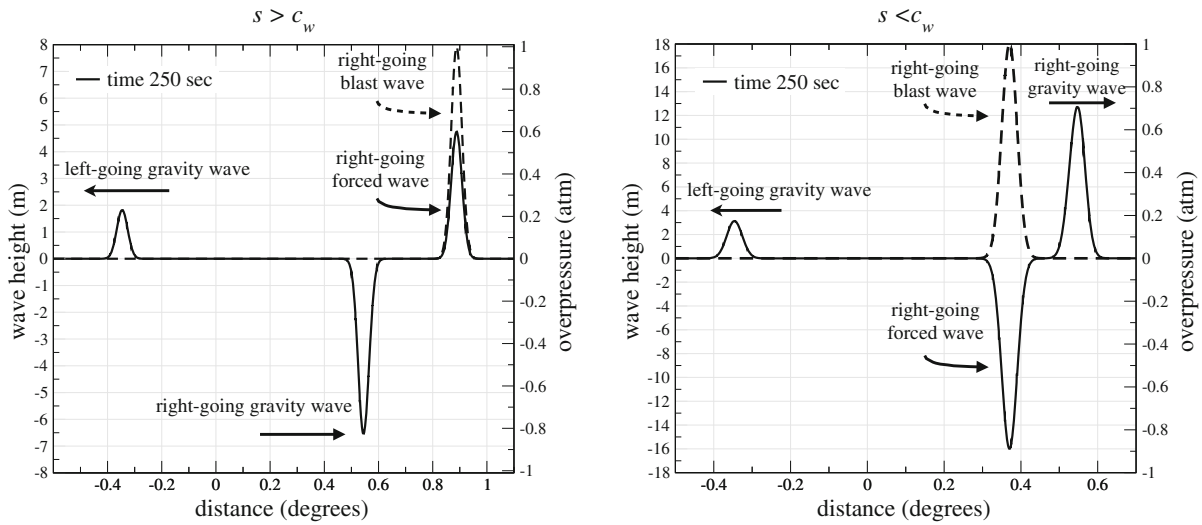

Figure 11

Numerical simulations showing wave heights h_r (left axis) and overpressure p_e (labeled on right axis). Left experiment uses $s > c_w$, on the right the pressure front is slower. On the left, the wave heights (solid line) under the pressure pulse (dashed line) are positive, as Eq. (6) predicts, and the tsunami wave trails the pressure wave. On the right, the pressure pulse is above a negative wave height (depression), and the tsunami leads the pressure wave

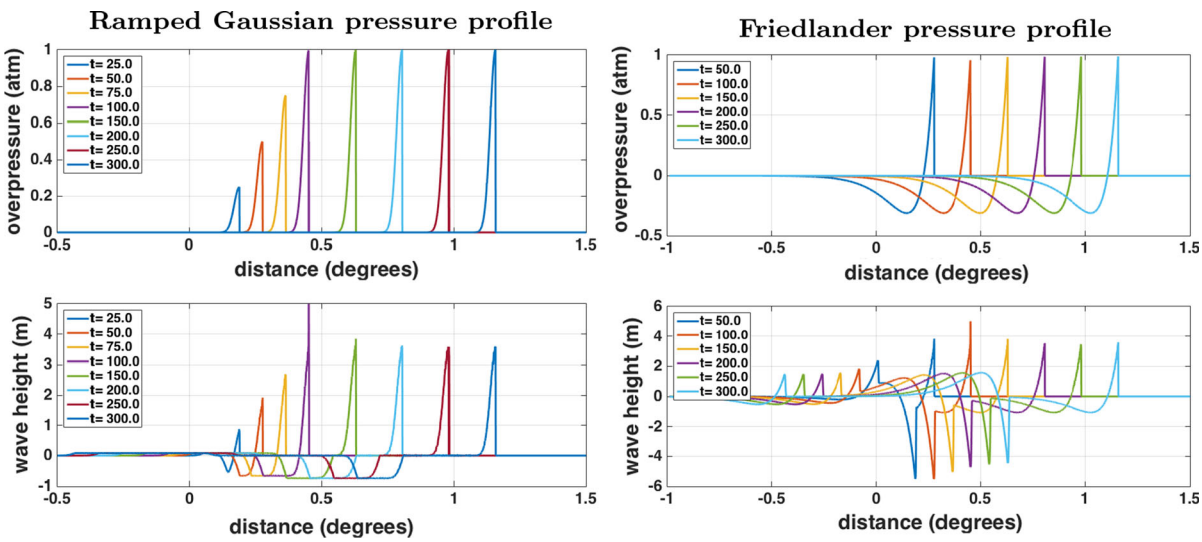

Figure 12

Left figure uses same high-speed Gaussian pressure pulse as in Fig. 11 but with the amplitude linearly ramped up over 100 s. Pressure profile shown on the top; bottom shows water wave heights. Right figure uses a Friedlander blast wave profile instead of a Gaussian. Both figures show the same positive forced water wave (since $s > c_w$) and the expected gravity waves from (8) but they take very different forms

response (5), and when the solution h exists. Dividing (5) by the shallow water speed $c_w^2 = gh_0$, and defining a function $f(H)$ equal to the left hand side, we get

$$f(H) = \frac{s^2}{2c_w^2}\left(1 - \frac{h_0^2}{h(m)^2}\right) + \left(1 - \frac{h(m)}{h_0}\right) = \frac{s^2}{2c_w^2}\left(1 - \frac{1}{H^2}\right) + (1 - H)) = \frac{p_e(m)}{\rho_w c_{\mathrm{w}}^2}, \tag{10}$$

where we define $H = h(m)/h_0$.

Figure 13 (left) shows a plot of $f(H)$, for overpressure traveling wave speeds s ranging from 0 to 400 m/s. This includes pressure waves both slower and faster than the water wave speed $c_w \approx 200$ m/s in a 4 km ocean. Note that there is a range where there is no solution to the equations. For an overpressure of 1 atmosphere, the right hand side of (10) is .0025. For the curve with $s = 350$ m/s, the maximum of $f(h) \approx 0.37$, so the equation will have a solution for a much stronger overpressure and/or a much shallower ocean basin. Between 0.8 and 1.2 (which corresponds to a wave response of 0.8 m), there is no solution for a right hand side of (10) outside of the range roughly between -1 and 1.

Figure 13 (right) shows a particular solution $h_r(m)$ for increasing overpressure amplitudes for a Gaussian traveling with speed $s = 350$ m/s in a 4 km deep ocean. As the amplitude of the forcing increases, the solution develops a cusp, and it appears that the derivative approaches infinity. This lack of a smooth solution could precede a bore.

4. Linearized Euler Model

In this section, we analyze a more complete model of the ocean's response to an airburst, to uncover possible shortcomings of the shallow water model of Sect. 3. We model the water using the Euler equations of a compressible fluid, which will bring in the effects of compressibility and dispersion. Another possibility would be to use one of the forms of the Boussinesq equations, but that also assumes incompressible flow, and would be more difficult to analyze. [See, however, a nice comparison of SWE and Serre–Green–Naghdi Boussinesq results in Popinet (2015).] We continue to neglect Coriolis forces, viscosity, friction, the Earth's curvature, etc. We linearize the Euler equations and the boundary conditions, since Fig. 10 suggests that linear approximations are reasonably accurate for these parameters.

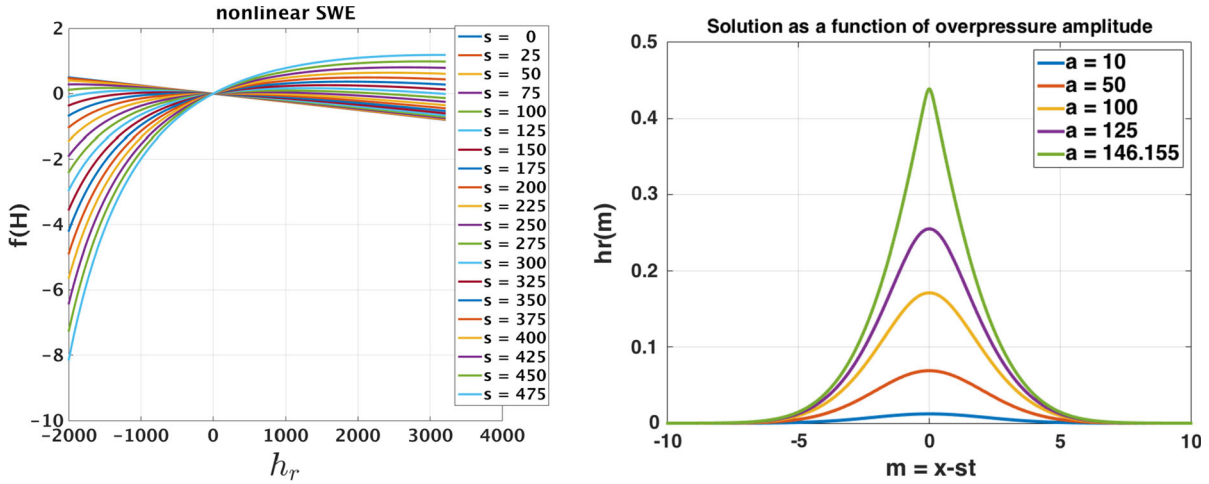

Figure 13
Left shows the region where a solution exists, for a given overpressure amplitude. Right shows the change in solution as the amplitude increases, at the fixed speed $s = 350$ m/s. When the cusp develops, there is no longer a smooth solution, corresponding to the region with no solution on the left plot

4.1. Derivation and Analysis

Our starting point for this section is the linearized Euler equations with linearized boundary conditions. A derivation is given in the Appendix. An explicit solution is not possible, and the results will depend instead on wave number. We will use wave number $k = \frac{2\pi}{L}$, where the length scale L for the atmospheric pressure wave is on the order of 10–20 km. This is very short relative to earthquake-generated tsunamis, which can have length scales on the order of 100 km or more. As before, those not interested in the analysis can skip to the end of the section for a summary of the main points.

The linearized Euler equations and boundary conditions that we use for analysis are

$$\begin{aligned} \widetilde{\rho}_t + \rho_w \widetilde{u}_x + \rho_w \widetilde{w}_z &= 0, \\ \rho_w \widetilde{u}_t + c_a^2 \widetilde{\rho}_x &= 0, \\ \rho_w \widetilde{w}_t + c_a^2 \widetilde{\rho}_z &= -\widetilde{\rho} g \ , \end{aligned} \tag{11}$$

where c_a is the speed of sound in water. (We use c_a for acoustic to distinguish it from the gravity wave speed $c_w = \sqrt{gh}$). Here, $\widetilde{\rho}$ is a small perturbation of ρ (and the same for the other variables), except for

$$h(x,t) = h_0 + h_r(x,t) \ .$$

where h_r is again the water's disturbance height for consistency with the previous section. The boundary conditions are

$$\text{bottom} : \widetilde{\mathrm{w}}(\mathrm{x}, \mathrm{z} = 0, \mathrm{t}) = 0, \tag{12}$$

$$\text{top} : \frac{\partial \mathrm{h_r}(\mathrm{x}, \mathrm{t})}{\partial \mathrm{t}} = \widetilde{w}(x, h_0, t) \tag{13}$$

$$\begin{aligned} \text{pressure bc:} \quad & c_a^2 \widetilde{\rho}(x, h_0, t) - \rho_w g\, h_r(x,t) \\ & = p_e(x,t). \end{aligned} \tag{14}$$

As in Sect. 3, we will assume the atmospheric pressure forcing has the form $p_e(x - st)$, and look for solutions of the same form, functions of $m = x - st$ and z. The system (11) becomes

$$-s\widetilde{\rho}_m + \rho_w \widetilde{u}_m + \rho_w \widetilde{w}_z = 0, \tag{15a}$$

$$-s\rho_w \widetilde{u}_m + c_a^2 \widetilde{\rho}_m = 0, \tag{15b}$$

$$-s\rho_w \widetilde{w}_m + c_a^2 \widetilde{\rho}_z = -\widetilde{\rho} g \ . \tag{15c}$$

The boundary conditions become

$$\widetilde{w}(m, 0) = 0, \tag{16a}$$

$$\widetilde{w}(m, h_0) = -s\, h_{r,m}(m), \tag{16b}$$

$$c_a^2 \widetilde{\rho}(m, h_0) = \rho_w g h_r(m) + p_e(m) \ . \tag{16c}$$

This system now includes the effects of dispersion and water compressibility.

These equations cannot be solved in closed form for general p_e. Therefore, we study the response using Fourier analysis. We will take a Fourier mode of the overpressure

$$p_e(m) = A_k e^{ikm} \ , \tag{17}$$

with amplitude A_k and compute the response as a function of m. The responses will have the form

$$h_r(m) = \widehat{h}_r \ e^{ikm}, \tag{18a}$$

$$\widetilde{\rho}(m,z) = \widehat{\rho}(z) e^{ikm}, \tag{18b}$$

$$\widetilde{u}(m,z) = \widehat{u}(z) e^{ikm}, \tag{18c}$$

$$\widetilde{w}(m,z) = \widehat{w}(z) e^{ikm} \ . \tag{18d}$$

The hat variables are the Fourier multipliers. The partial differential equations (15a–15c) become ordinary differential equations with wave number k as a parameter.

Note that (15b) depends only on derivatives with respect to m. Integrating it gives

$$-s\rho_w \widetilde{u} + c_a^2 \widetilde{\rho} = 0.$$

The constant of integration is zero for each z since as $m \to \infty$ we know $\widetilde{u} = 0$ and $\widetilde{\rho} = 0$. This gives an expression for $\widetilde{\rho}$ in terms of $\widetilde{u}$,

$$\widetilde{\rho} = \frac{s\rho_w \widetilde{u}}{c_a^2}, \tag{19}$$

which we can use in (15a) and (15c). After substituting for $\widetilde{\rho}$ and dividing by ρ_w, the remaining system of two equations is

$$\begin{aligned} \widetilde{u}_m \left(1 - \frac{s^2}{c_a^2}\right) + \widetilde{w}_z &= 0, \\ -\widetilde{w}_m \quad + \widetilde{u}_z &= -\frac{g}{c_a^2} \widetilde{u}. \end{aligned} \tag{20}$$

Substituting the Fourier modes (18c–18d) into (20)

and differentiating $\widetilde{u}$ and $\widetilde{w}$ with respect to m give an ordinary differential equation in z for the velocities,

$$\begin{pmatrix} \widehat{u} \\ \widehat{w} \end{pmatrix}_z = \begin{pmatrix} -g/c_a^2\,\widehat{u} + i\,k\,\widehat{w} \\ -i\,k\,\widehat{u}\,(1 - s^2/c_a^2) \end{pmatrix} = \begin{bmatrix} -g/c_a^2 & i\,k \\ -i\,k\,(1 - s^2/c_a^2) & 0 \end{bmatrix} \begin{pmatrix} \widehat{u} \\ \widehat{w} \end{pmatrix} . \quad (21)$$

The general solution to this 2-by-2 system is the linear combination

$$\begin{pmatrix} \widehat{u} \\ \widehat{w} \end{pmatrix} = a_+ \mathbf{v}_+ e^{\mu_+ z} + a_- \mathbf{v}_- e^{\mu_- z} , \quad (22)$$

where $\mu_\pm$ and $\mathbf{v}_\pm$ are the eigenvalues and eigenvectors of the matrix in (21), and the scalar coefficients $a_\pm$ are chosen to satisfy the boundary conditions. The eigenvalues are

$$\mu_\pm = \frac{\frac{-g}{c_a^2} \pm \sqrt{\frac{g^2}{c_a^4} + 4k^2(1 - s^2/c_a^2)}}{2} . \quad (23)$$

The eigenvectors (chosen to make the algebra easier so they are not normalized) are

$$\mathbf{v}_+ = \begin{pmatrix} \frac{2\mu_+}{-ik} \\ 2(1 - s^2/c_a^2) \end{pmatrix}, \quad \mathbf{v}_- = \begin{pmatrix} \frac{2\mu_-}{-ik} \\ 2(1 - s^2/c_a^2) \end{pmatrix}. \quad (24)$$

The boundary condition at $z = 0$ is (16a). To apply it, note that $\widehat{w}$ corresponds to the second component of the eigenvectors $\mathbf{v}_\pm$. We find that $a_+ = -a_-$. Henceforth, we call this coefficient simply a.

Next, we substitute the Fourier modes (18c–18d) into the remaining boundary conditions (16b) and (16c). We use the pressure forcing equation (17) in the form $\widehat{p}_e = A_k$. The result is

$$\widehat{w}(h_0) = -iks\,\widehat{h}_r, \quad (25a)$$

$$c_a^2 \widehat{\rho}(h_0) - \rho_w g \widehat{h}_r = A_k . \quad (25b)$$

Using equation (19) to substitute $\widehat{\rho} = \frac{s\rho_w}{c_a^2}\widehat{u}$ in (25b) gives an expression for $\widehat{h}_r$

$$\widehat{h}_r = \frac{s}{g}\widehat{u} - \frac{A_k}{\rho_w g} . \quad (26)$$

This can be used to replace $\widehat{h}_r$ in (25a) to get

$$\widehat{w}(h_0) = \frac{-iks^2}{g}\widehat{u}(h_0) + \frac{iksA_k}{\rho_w g} . \quad (27)$$

The final steps are using the form of the solution (22) in (27) to solve for the coefficient a. With this, everything is known, and $\widehat{u}$, $\widehat{w}$ and the response height $\widehat{h}_r$ can be evaluated.

Putting it all together, we get

$$2\,a(1 - s^2/c_a^2)\left(e^{\mu_+ h_0} - e^{\mu_- h_0}\right) = \frac{iks^2}{g}\frac{2\,a}{-ik}\left(\mu_+ e^{\mu_+ h_0} - \mu_- e^{\mu_- h_0}\right) + \frac{iksA_k}{\rho_w g} . \quad (28)$$

Grouping terms, the final expression to solve for a (using the definition (23) for $\mu_\pm$) is given by

$$2a\left[(1 - s^2/c_a^2)\left(e^{\mu_+ h_0} - e^{\mu_- h_0}\right) + \frac{s^2}{g}\left(\mu_+ e^{\mu_+ h_0} - \mu_- e^{\mu_- h_0}\right)\right] = \frac{iksA_k}{\rho_w g} \quad (29)$$

To summarize, given an overpressure amplitude A_k with wavelength k, equation (29) gives the scalar coefficient a in the velocity equations, then we solve for $\widehat{u}$ and $\widehat{w}$ using (22), and use (26) to get the Fourier multiplier for the wave height response.

4.2. *Linearized Euler Model Computations*

We evaluate these results using the following parameters: an ocean with depth $h_0 = 4$ km , ocean sound speed $c_a = 1500$ m/s, $\rho_w = 1025$ kg/m ^{3}, and atmospheric overpressure of $A_k = 1$ atm with pressure wave speed $s = 350$ m/s, faster than the gravity wave speed of about 200 m/s. The responses are linear in the overpressure amplitude A_k, so we do not evaluate these curves for any other overpressures.

Figure 14 (left) shows the surface wave height $\widehat{h}(k)$ as a function of length scale L, and (right) the amplitude of the surface velocities $\widehat{u}(h_0, k)$ and $\widehat{w}(h_0, k)$ are shown. There are two curves in each plot: one uses the physical acoustic water wave speed of $c_a = 1500$ m/s, and the other uses a very large non-physical acoustic speed in the water of $c_a \times 10^8$. The latter corresponds to the intermediate model of finite depth but incompressible water. This should, and does, asymptote in the long wave ($k \to 0$) limit to the result of the shallow water equations. The difference

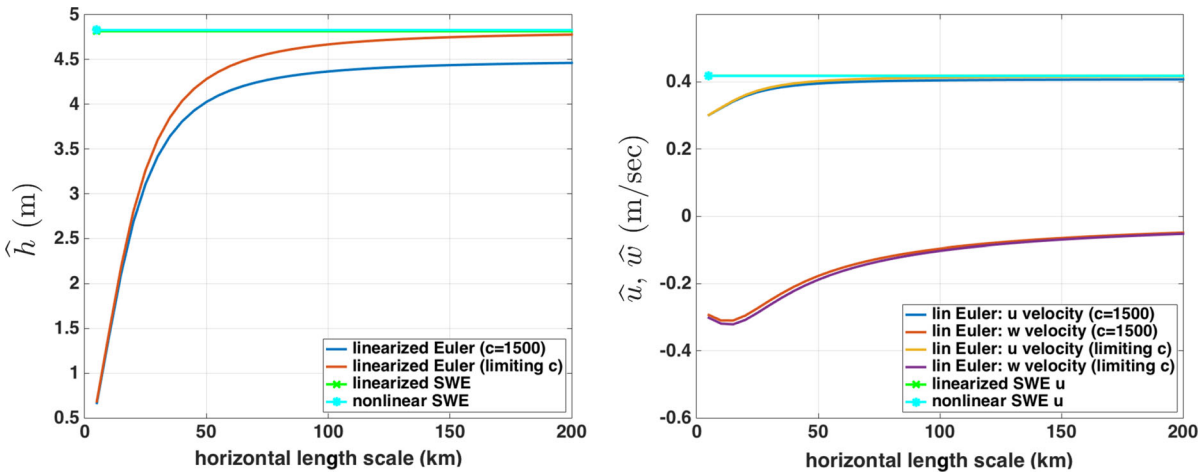

Figure 14
Left figure shows wave height $\widehat{h}(k)$ as a function of wavelength for the linearized Euler equations using an atmospheric overpressure of 1 atmosphere. Also shown is the shallow water solution from Sect. 3. Right figure shows the u and w velocities. Both plots show curves using the physical sound speed of $c_a = 1500$ m/s, and the limiting infinite speed solution. Both figures use the parameters $h_0 = 4$ km, and 1 atmosphere overpressure

between the blue and green curves shows approximately a 20% reduction in the amplitude of the longer length scales due to compressibility (but that this is not the amplitude of the total wave response yet). Note also that the u velocity asymptotes to the shallow water limit, and the w velocity approaches zero. The velocity curves show less of an effect due to compressibility.

For atmospheric forcing from asteroids with airbursts, the length scales of interest are closer to the short end, perhaps 10 or 20 km. In this regime, the compressibility effects are around 10% or less. But at these wavelengths, dispersive effects reduce the response predicted by shallow water theory by nearly half!

This becomes more clear by comparing the forced wave response to a Gaussian pressure pulse instead of using just a single frequency. We use the pressure pulse form (7) as before but with length scale 5 (not $\sqrt{5}$), take the Fourier transform, multiply by the Fourier multipliers shown in Fig. 14, and transform back. Figure 15 shows the results for two different water depths h_0: 4 km and 1 km. The blue curve uses the water wave speed c_a=1500 m/s, and the red curve uses the limiting c_a. Compressibility changes the height by less than 10% in Fig. 15 for both depths. However, in the deeper water, the shallow water response is almost 70% larger than either Euler solution, and has a narrower width. One can think of this in two ways. The broader response from linearized Euler is a result of dispersion, which makes things spread. Alternatively, it is the result of filtering out the shorter wavelengths needed to make a narrow Gaussian. In the right figure, the water is shallower, and the linearized Euler results are closer to the shallow water results.

In Fig. 16, we fix the horizontal length scale at 15 km and instead vary the speed of the pressure wave s. This figure again uses $h_0 = 4000$ m, and $c_a = 1500$ m/s. Three curves are shown: the linearized Euler, and the nonlinear and linearized shallow water responses. There is much more difference in this set of curves, particularly around the regions where resonance occurs. Here too we see that the wave height response to the linearized Euler forcing is negative for pressure forcing speeds $s \lesssim 150$ m/s and again unintuitively, positive for larger s. There is also a section of the red curve that is missing, corresponding to the regions where there is no smooth solution. Note also that the overpressure speed where the resonance occurs is significantly slower for the linearized Euler than for the SWE.

5. Conclusions

We have presented several numerical simulations using the shallow water equations over real

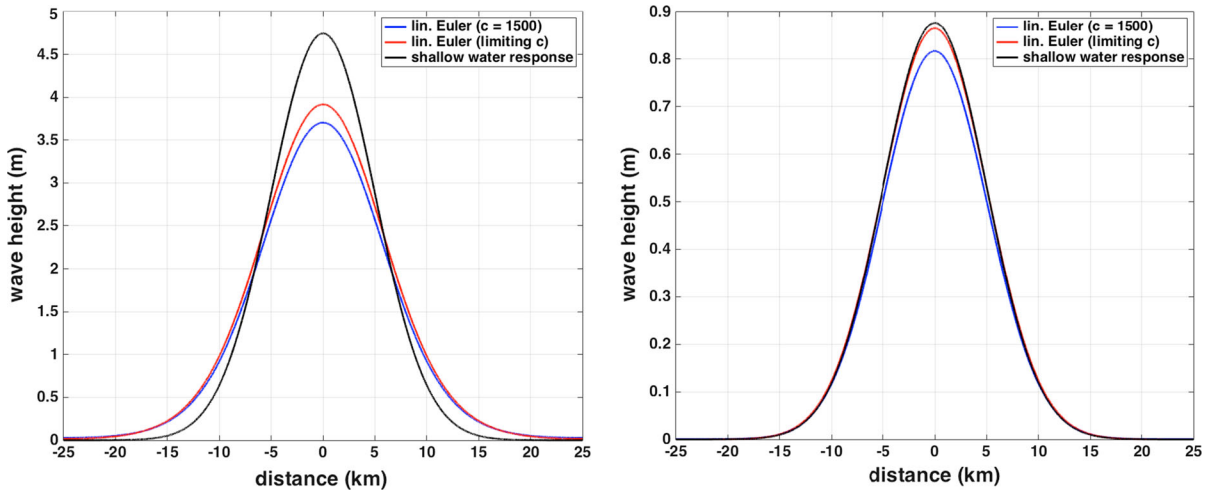

Figure 15
Response to a Gaussian pressure pulse for the linearized Euler equations, using the actual sound speed $c_a = 1500$ m/s, and a limiting sound speed that mimics the incompressible case. The shallow water response is also shown. Left uses depth $h_0 = 4$ km; right uses $h_0 = 1$ km, so it is closer to a shallow water wave. Both use a maximum overpressure of 1 atm

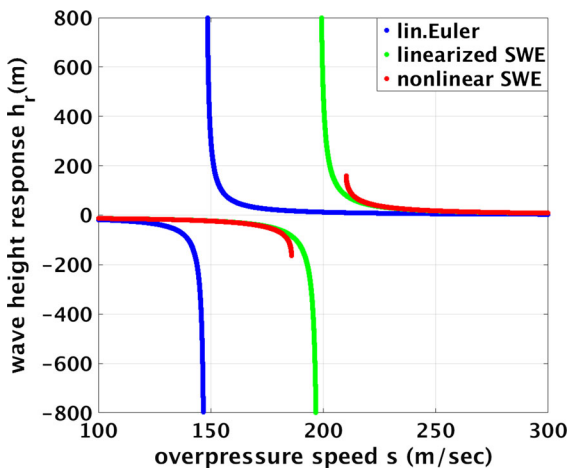

Figure 16
Wave height response as a function of s, the speed of the overpressure front. The depth h_0 is a constant 4 km, and the length scale is held fixed at 15 km. There is a large variation between the models, especially in the location where resonances occur

bathymetry that demonstrate the ocean's response to a 250MT airburst. There is no significant wave response from the ocean, in either the forced wave or the gravity waves after a short distance. Our calculations show that the amplitude of the pressure wave response decreases much more rapidly than the gravity waves do. The blast had to be very close to shore to get a sizeable response. Thus the more serious danger from an airburst is not from the tsunami, but from the local effects of the blast wave itself.

Several unexpected features found in the simulations were explained using a one-dimensional model problem with a traveling wave solution for the SWE. One of the main results, that the wave response height is proportional to the depth of the water, explains why putting the blast on a continental shelf close to shore did not generate more inundation than putting it further away in deeper water.

We also looked at the water's response to an airburst using the linearized Euler equations. In this case, the traveling wave model problem shows that the amplitudes of the important wave numbers in the ocean's response are greatly decreased. We do not yet know what this means for the gravity wave response. In addition, we expect the character of the water's response to be different, since dispersive waves will generate a wave train characterized by multiple peaks and troughs. The effect of this on land, and whether it causes inundation when the SWE response does not, is something we plan to investigate in the future.

Acknowledgements

We are particularly grateful to Mike Aftosmis, Oliver Bühler, and Randy LeVeque for more in-depth discussions. It is a pleasure to thank our colleagues at the Courant Institute for several lively discussions. We thank Michael Aftosmis for providing the blast wave ground footprint model. This effort was partially supported through a subcontract with Science and Technology Corporation (STC) under NASA Contract NNA16BD60C.

Appendix

In this appendix we start with the nonlinear Euler equations for a compressible inviscid fluid with nonlinear boundary conditions at the interface between ocean and air. The static unforced solution to these equations is determined by hydrostatic balance. The hydrostatic pressure is p_0, and the hydrostatic density is ρ_0. Since the static density variation is small (under 2%), we will end up neglecting it and proceed to linearize the equations, deriving Eq. (11)–(14) in Sect. 4.

This time there are two spatial coordinates, a horizontal coordinate x, and a vertical coordinate z. The (flat) bottom is $z = 0$. The moving top surface is $z = h(x,t)$. The horizontal and vertical velocity components are u and w respectively, and the water density is denoted by ρ. The Euler equations are

$$\begin{aligned} \rho_t + (\rho u)_x + (\rho w)_z &= 0, \\ (\rho u)_t + (\rho u^2 + p)_x + (\rho u w)_z &= 0, \\ (\rho w)_t + (\rho u w)_x + (\rho w^2 + p)_z &= -\rho g. \end{aligned} \tag{30}$$

There is a "no flow" boundary condition at the bottom boundary,

$$w(x, z = 0, t) = 0. \tag{31}$$

The kinematic condition at the top boundary Whitham (1974) states that a particle that moves with the surface velocity stays on the surface,

$$h_t + u h_x = w(x, h(x,t), t)\,. \tag{32}$$

The dynamic boundary condition at the top is continuity of pressure,

$$p(x, h(x,t), t) = p_{\text{atm}} + p_e(x,t)\,. \tag{33}$$

The left side of (33) is pressure in the water evaluated at the top boundary. The right side is the atmosphere's ambient pressure, which is the sum of the static background atmospheric pressure p_{atm} and the dynamic blast wave overpressure $p_e(x,t)$.

For static solutions ($p_e = 0$, $u = w = 0$), the nonlinear Eq. (30) reduce to the hydrostatic balance condition

$$\frac{dp_0}{dz} = -g\rho_0(z)\,. \tag{34}$$

Let the water density ρ_w be the density at the water surface. If the density differences are small (as they turn out to be), we may use a linear approximation to the equation of state,

$$p(\rho) = p(\rho_w) + c_a^2(\rho - \rho_w)\,,$$

where c_a is the acoustic sound speed in water at density ρ_w, $c_a^2 = \frac{dp}{d\rho}(\rho_w)$. The behavior of $\rho_0(z)$ is found by substituting this into (34): $\frac{dp_0}{dz} = c_a^2 \frac{d\rho_0}{dz} = -g\rho_0$. Therefore, for any two heights z_1 and z_2, we have

$$\rho_0(z_2) = \rho_0(z_1) e^{-\frac{g}{c_a^2}(z_2 - z_1)}\,.$$

If $z_2 - z_1 = 4$ km , and $c_a = 1500$ m/s, then $\frac{g}{c_a^2}(z_2 - z_1) < .02$. Therefore, the density varies by less than about 2% between the water surface and bottom.

We denote small disturbance quantities with a tilde, except for the wave height response h_r, which we use for continuity with the previous sections. For example, the water density is $\rho_0(z) + \widetilde{\rho}(x,z,t)$. These disturbances are driven by the atmospheric overpressure $p_e(x,t)$. We substitute the expressions $\rho = \rho_0 + \widetilde{\rho}$, $u = \widetilde{u}$, $w = \widetilde{w}$ (since the velocities are linearized around zero), and $p = p_0 + c_a^2\widetilde{\rho}$ into the Euler Eq. (30) and calculate up to linear terms in the

disturbance variables. Using the hydrostatic balance condition (34), this gives

$$\begin{aligned} \widetilde{\rho}_t + \rho_0 \widetilde{u}_x + \rho_0 \widetilde{w}_z &= 0, \\ \rho_0 \widetilde{u}_t + c_a^2 \widetilde{\rho}_x &= 0, \\ \rho_0 \widetilde{w}_t + c_a^2 \widetilde{\rho}_z &= -\widetilde{\rho} g \, . \end{aligned}$$

Finally, we replace the (slightly) variable $\rho_0(z)$ with the constant ρ_w. The resulting equations, which we use for analysis, are

$$\begin{aligned} \widetilde{\rho}_t + \rho_w \widetilde{u}_x + \rho_w \widetilde{w}_z &= 0, \\ \rho_w \widetilde{u}_t + c_a^2 \widetilde{\rho}_x &= 0, \\ \rho_w \widetilde{w}_t + c_a^2 \widetilde{\rho}_z &= -\widetilde{\rho} g \end{aligned} \quad . \tag{35}$$

The bottom boundary condition (31) is already linear. For the top boundary conditions, we express the water height as the sum of the background height h_0 and the disturbance height h_r:

$$h(x,t) = h_0 + h_r(x,t) \, .$$

To leading order in h_r, $\widetilde{u}$ and $\widetilde{w}$, the linear approximation to the kinematic boundary condition (32) is

$$\frac{\partial h_r}{\partial t}(x,t) = \widetilde{w}(x, h_0, t) \ . \tag{36}$$

For the dynamic boundary condition (33), which was $p(x, h(x,t), t) = p_{\text{atm}} + p_e$, we use the Taylor expansion and the perturbation approximation

$$\begin{aligned} p(x, h(x,t), t) &\approx p(h_0) \ + \ p_{0,z}(h_0)\, h_r(x,t) \\ &\approx p_0(h_0) + \widetilde{p}(x, h_0, t) + p_{0,z}(h_0)\, h_r(x,t) \\ &\approx p_0(h_0) + c_a^2 \widetilde{\rho}(x, h_0, t) + p_{0,z}(h_0)\, h_r(x,t) \end{aligned} \quad .$$

For the undisturbed quantities, the pressure at the top is $p(h_0) = p_{\text{atm}}$. The hydrostatic balance relation (34) in the water (applied at the top) is $p_{0,z}(h_0) = -g\rho_w$. Making these substitutions gives

$$p_0(h_0) + c_a^2 \widetilde{\rho} + p_{0,z} h_r = p_{\text{atm}} + p_e \, , \tag{37}$$

giving the result

$$c_a^2 \widetilde{\rho}(x, h_0, t) - \rho_w g \, h_r(x,t) = p_e(x,t) \, . \tag{38}$$

Summarizing, the linearized Euler equations are (35), with linearized boundary conditions (31), (36) and (38).

References

Aftosmis, M., Mathias, D., Nemec, M., Berger, M.: Numerical simulation of bolide entry with ground footprint prediction. AIAA-2016-0998 (2016)

GeoClaw Web Site. http://www.clawpack.org/geoclaw. http://www.geoclaw.org/ (2017)

George, D. (2008). Augmented Riemann solvers for the shallow water equations over variable topography with steady states and inundation. *J. Comp. Phys.*, *227*(6), 3089–3113.

Gica, E., Arcas, D., & Titov, V. (2014). *Tsunami inundation modeling of Ocean Shores and Long Beach*. NOAA Center for Tsunami Research, Pacific Marine Environmental Laboratory: Washington due to a Cascadia subduction zone earthquake. Tech. rep.

Gisler, G. (2008). Tsunami simulations. *Annu. Rev. Fluid Mech.*, *40*, 71–90.

Gisler, G., Weaver, R., & Gittings, M. (2010). Calculations of asteroid impacts into deep and shallow water. *Pure Appl. Geophys.*, *168*, 1187–1198.

González, F.I., LeVeque, R.J., Chamberlain, P., Hirai, B., Varkovitzky, J., George, D.L.: Geoclaw model. In: Proceedings and Results of the 2011 NTHMP Model Benchmarking Workshop, pp. 135–211. National Tsunami Hazard Mitigation Program, NOAA (2012). http://nthmp.tsunami.gov/documents/nthmpWorkshopProcMerged.pdf

Harkrider, D., & Press, F. (1967). The Krakatoa air-sea waves: an example of pulse propagation in coupled systems. *Geophys. J. R. Astr. Soc.*, *13*, 149–159.

Kranzer, H., & Keller, J. (1959). Water waves produced by explosions. *J. Appl. Phys.*, *30*(3), 398–407.

LeVeque, R. (1997). Wave propagation algorithms for multidimensional hyperbolic systems. *J. Comput. Phys.*, *131*, 327–353.

LeVeque, R., George, D., Berger, M.: Tsunami modelling with adaptively refined finite volume methods. Acta. Numerica. pp. 211–289 (2011)

Liu, P. (2009). Tsunami modeling: propagation. In E. Bernard & A. Robinson (Eds.), *The sea: Tsunamis* (pp. 295–320). Cambridge: Harvard University Press.

Mandli, K.: Finite volume methods for the multilayer shallow water equations with applications to storm surges. Ph.D. thesis, University of Washington (2011)

Melosh, H.: Impact-generated tsunamis: an over-rated hazard. In: 34th Lunar and Planetary Sciences Conference Abstract (2003)

Monserrat, S., Vilibic, I., & Rabinovich, A. (2006). Meteotsunamis: atmospherically induced destructive ocean waves in the tsunami frequency band. *Nat. Hazards Earth Syst. Sci.*, *6*, 1035–1051.

Morrison, D., Venkatapathy, E.: Asteroid generated tsunami: summary of NASA/NOAA workshop. Tech. Rep. NASA/TM-2194363, NASA Ames Research Center (2017)

Petersen, M., Cramer, C., & Frankel, A. (2002). Simulations of seismic hazard for the Pacific northwest of the United States from earthquakes associated with the Cascadia subduction zone. *Pure Appl. Geophys.*, *159*, 2147–2168.

Popinet, S. (2015). A quadtree-adaptive multigrid solver for the Serre-Green-Naghdi equations. *J. Comp. Phys.*, *302*, 336–358.

Popova, O., Jenniskens, P., Emelyanenko, V., Kartashova, A., Biryukov, E., et al. (2013). Chelyabinsk airburst, damage

assessment, meteorite recovery, and characterization. *Science*, *342*(6162), 1069–1073. https://doi.org/10.1126/science.1242642.

Proudman, J. (1929). The effects on the sea of changes in atmospheric pressure. *Geophys. Suppl. Mon. Not. R. Astron. Soc.*, *2*(4), 197–209.

Uslu, B., Eble, M., Titov, V., Bernard, E.: Distance tsunami threats to the ports of Los Angeles and Long Beach, California. Tech. rep., NOAA Center for Tsunami Research, Pacific Marine Environmental Laboratory (2010). NOAA OAR Special Report, Tsunami Hazard Assessment Special Series (2)

Vreugdenhil, C. (1994). *Numerical methods for shallow-water flow*. Dordrecht: Kluwer Academic Publishers.

Weiss, R., Wünnemann, K., & Bahlburg, H. (2006). Numerical modelling of generation, propagation and run-up of tsunamis caused by oceanic impacts: model strategy and technical solutions. *Geophys. J. Intl.*, *167*, 77–88.

Whitham, G. B. (1974). *Linear and nonlinear waves*. Hoboken: John Wiley & Sons.

(Received April 12, 2017, revised October 28, 2017, accepted December 1, 2017, Published online December 18, 2017)